Sound Generation and Radiation from Rotor Tip-Vortex Pairing Phenomenon

Ki Hoon Chung*
Korea Aerospace Research Institute, Daejeon 305-333, Republic of Korea
Jae Wook Kim†
University of Southampton, Southampton, England SO17 1BJ, United Kingdom
Ki Wahn Ryu‡
Chonbuk National University, Jeonbuk 561-756, Republic of Korea
Kyung Tae Lee§
Sejong University, Seoul 143-747, Republic of Korea
and
Duck Joo Lee¶
Korea Advanced Institute of Science and Technology, Daejeon 305-701, Republic of Korea

Sound generation and radiation from rotor tip–vortex pairing are calculated numerically. Wake geometries of a two-bladed rotor in axial flights are calculated using a time-marching free-wake method without a nonphysical model of the far wake. The acoustic field can be obtained using acoustic analogy. To show the accuracy of the flow calculation scheme, the tip-vortex geometries of the present calculation are compared with those done in the previous publication of a small-scaled rotor experiment. The accuracy of the vortex sound calculation scheme is validated by comparing its numerical and the analytic solution of circular vortex-ring interaction. The tip-vortex pairing consists of a turn of the tip-vortex from one blade rolling around the tip-vortex from the other blade. The tip-vortex pairing amplifies the noise and generates new dominant frequencies. The tip-vortex pairing noise has a quadrupole directivity pattern, and it is especially dominant in the direction of the rotation axis. The peak components of the noise spectrum represent the pairing period and an instability mode.

Nomenclature

A_{ij}	=	influence coefficient matrix, 1/m
a_0	=	ambient acoustic velocity, m/s
$C(\xi)$	=	parabolic blending curve
$G(\boldsymbol{x}, \boldsymbol{y}, t - \tau)$	=	free space Green function
$\boldsymbol{n}(\boldsymbol{x}, t)$	=	vector normal to the moving surface
p	=	acoustic pressure
$p(r), q(s)$	=	parametric parabolas
q	=	acoustic source term
R_i	=	normal induced velocity at each control point, m/s
$\boldsymbol{V}(\boldsymbol{x}, t)$	=	blade surface velocity, m/s
$\boldsymbol{V}_{\text{wake}}(\boldsymbol{x}, t)$	=	induced velocity resulting from the vorticity field in the wake, m/s
Γ_j	=	circulation value of the blade vortex lattice
μ	=	doublet strength
μ_0	=	Rosenhead cutoff parameter
ρ_0	=	ambient air density
σ	=	source strength
τ	=	retarded time $(t - |\boldsymbol{x} - \boldsymbol{y}|/a_0)$, s
$\Phi(\boldsymbol{x}, t)$	=	velocity potential over the entire flowfield, excluding the solid boundaries and wakes
ω	=	vorticity in flowfield

Introduction

IN recent years, rotor noise reduction has become an increasingly important research subject for the design of a quiet helicopter. The high noise levels in rotor noise are caused by an impulsive noise-generating mechanism known as the blade–vortex interaction (BVI) that results from the close proximity between the rotor blades and the vortices. In the past 15 years, considerable progress has been made in understanding as well as predicting the helicopter rotor BVI noise. It was revealed that the key to accurate rotor BVI noise prediction is the accurate prediction of rotor airloads. There has been moderate success in the prediction of rotor BVI noise. However, these prediction programs have not yet been extensively applied or validated for the cases in which the tip vortices shed from a helicopter rotor interact with each other significantly. To accurately predict the total noise including the BVI noise, one has to account for all the noise sources for a helicopter rotor. The vortex–vortex interaction (VVI) noise due to tip-vortex pairing should be included in the rotor noise prediction program.

Landgrebe[1] and Tangler et al.[2] first observed that the tip vortices shed from a two-bladed rotor could interact with each other significantly. Widnall[3] and Gupta and Loewy[4] tried to analyze this pairing phenomenon using linear stability theory. Recent experiments[5,6] showed more detailed procedures for tip-vortex pairings. Sound generated from an unsteady vortical flow has been studied by many researchers.[7–10] The acoustic field can be obtained by using an acoustic analogy or by matched asymptotic expansion. It is shown that the sound source term at low Mach number is linearly dependent on the third-order derivatives of the vorticity distributions and their position vectors. Therefore, to obtain the sound pressure accurately, detailed descriptions of the vortex motion are required.
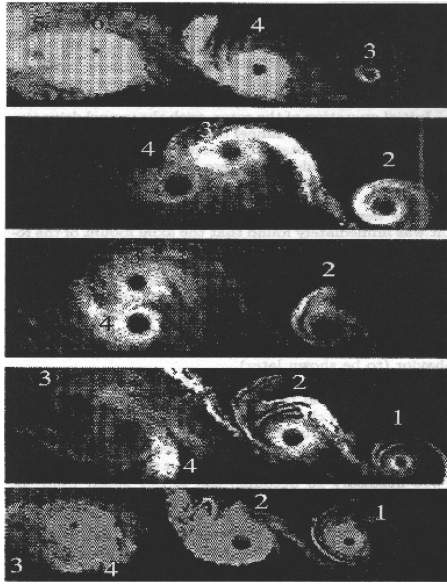
Fig. 1 Sequence of tip-vortex pairing from the individual blade, 9-deg collective, 3.5-fps climb rate.[6]

The tip-vortex pairing motion is three-dimensional, unsteady, and highly nonlinear because of the differing curvature along the tip-vortex line. Hence, it is necessary to develop a numerical method with high resolution, describing the distorted vortex motion in detail.[10,11] It is obvious that numerical errors in the vortex motion may lead to misinterpretations of the calculated acoustic data.

The aim of this paper is to study the noise generated from the tip-vortex pairing motion in comparison with the rotor noise.

Tip–Vortex Pairing

Figure 1 shows a sequence of images of tip vortex development at a rotor collective angle of 9 deg and the climb rate of 3.5 fps (1.067 m/s). The vortices from the two blades are identified by their numbers; that is, an odd-numbered vortex belongs to one blade and an even-numbered to the other. The time spacing between successive frames is not constant, but it was chosen to show the progress of the pairing phenomena. The first frame shows two clear vortices, marked "3" and "4." In the next frame, the vortex 3 has begins to roll up with 4. This process continues through the next two frames, until 3 and 4 have essentially interchanged their positions while moving downstream (left direction in Fig. 1).

Flowfields

The fluid surrounding a body is assumed to be inviscid, irrotational, and incompressible over the entire flowfield, excluding the body's solid boundaries and its wakes. Therefore, a velocity potential $\Phi(x, t)$ can be defined and the continuity equation in the inertial frame becomes

$$\nabla^2 \Phi = 0 \tag{1}$$

The boundary condition requiring zero normal velocity across the body's solid boundaries is

$$(\nabla \Phi + V_{\text{wake}} - V) \cdot n = 0 \tag{2}$$

where $V_{\text{wake}}(x, t)$ is the induced velocity due to the vorticity field in the wake, $V(x, t)$ is the body surface's velocity, and $n(x, t)$ is the vector normal to the moving surface, as viewed from the blade.

Using Green's second identity, the general solution of Eq. (1) can be constructed by integrating the contribution of the basic solution of source (σ) and doublet (μ) distributions over the body's surface:

$$\Phi(x, t) = \frac{1}{4\pi} \int_{\text{body}+\text{wake}} \mu n \cdot \nabla \left(\frac{1}{r}\right) ds - \frac{1}{4\pi} \int_{\text{body}} \sigma \left(\frac{1}{r}\right) ds \tag{3}$$

Inserting Eq. (3) into Eq. (2) gives

$$\left\{ \frac{1}{4\pi} \int_{\text{body}+\text{wake}} \mu \nabla \left[\frac{\partial}{\partial n} \left(\frac{1}{r}\right) \right] ds \right.$$

$$\left. - \frac{1}{4\pi} \int_{\text{body}} \sigma \nabla \left(\frac{1}{r}\right) ds - V \right\} \cdot n = 0 \tag{4}$$

The source term is neglected in the case of the thin blade. Thus, only the first part of Eq. (3) is used to represent the lifting surface. The constant-strength doublet panel is equivalent to a closed vortex lattice with the same strength of circulation ($\Gamma = \mu$). Then the induced velocity of the vortex lattice in Eq. (4), representing the blade, can be obtained using the Biot–Savart law:

$$V = -\frac{1}{4\pi} \int_c \frac{r \times \Gamma dl}{|r|^3} \tag{5}$$

The collocation point is at the midspan and three-quarter chord of each. The boundary condition of no-flow penetration is satisfied at the collocation point of each lattice. The application of the flow tangency condition (Eq. 4) to the vortex lattice distribution yields the following linear matrix equation to be solved:

$$A_{ij} \Gamma_j = R_i \qquad (i, j = 1, \ldots, n) \tag{6}$$

where A_{ij} is the coefficient matrix of the normal induced velocity on the ith element of the blade due to the jth vortex lattice with unit circulation, and Γ_j is the unknown circulation value of the blade vortex lattice. R_i is the normal induced velocity at each control point due to the freestream velocity, the blade velocity, and the wake-induced velocity.

Time-Marching Free-Wake Method

A three-dimensional wing trails the bound circulation Γ into the wake. The radial variation of the bound circulation produces trailed vorticity in the wake, where its direction is parallel to the local freestream direction at each instant it leaves the blade. The azimuthal variation of the bound circulation produces the shed vorticity, oriented radially in the wake. The strengths of the trailed and shed vorticity are determined by the radial and azimuthal derivatives of the bound circulation at the time the wake element leaves the blade. The bound circulation has a peak near the tip and quickly drops to zero. The trailed sheet therefore has a high strength (proportional to the radial derivative of Γ) at the outer wake, and quickly rolls up into a concentrated tip vortex. The strength of the trailed shed wake vortex at this time step is set equal to that of the vortex lattice elements, which is located at the trailing edge of the blade ($\Gamma_{\text{T.E},t} = \Gamma_{\text{wake},t}$). This condition is forced to satisfy the Kutta condition ($\gamma_{\text{T.E}} = 0$).

Because the wake surface is force-free, each vortex wake element moves with the local stream velocity, which is induced by the other wake element and the blade. The convection velocity of the wake is calculated in the inertial frame. The vortex wakes are generated at each time step. Therefore, the number of wake elements increases as the blade is rotating. It is clear that a large number of line elements for highly curved and distorted wake regions such as the tip vortex are necessary to describe the vortex filament distortions accurately. In general, the computational time for the calculation of the wake distortion is proportional to the square of the vortex element number. Therefore, a curved element is used to reduce the number of elements.

Parabolic Blending Curve Interpolations

There are many mathematical expressions to represent the three-dimensional curves. Generally, cubic splines are used to describe the curves. However, cubic splines have some disadvantages; they require a large tridiagonal matrix inversion, and the numerical disturbance of position in any one segment affects all of the global curve segments. Therefore, the curve is not adequate to represent the vortex filament motion in strong interaction problems. Parabolic
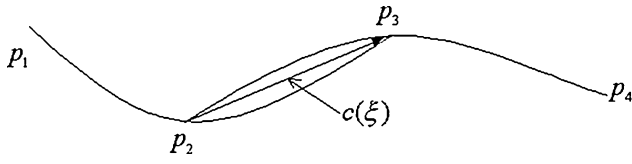
Fig. 2 Parabolic blending method.

blending, employed here, maintains the continuity of the first derivative in space, which is critical to the self-induced vortex interactions and the interactions with the wakes and blade. The parabolic blending curve $C(\xi)$ is given by

$$C(\xi) = (1 - \xi)p(r) + \xi q(s) \tag{7}$$

The functions $p(r)$ and $q(s)$ are parametric parabolas through P_1, P_2, P_3 and P_2, P_3, P_4 as shown in Fig. 2, respectively.

A generalized parametric blending curve is developed from the assumption of the normalized chord length approximation for the position parameters, r at P_2 and s at P_3, which are linearly related to the parameter ξ in the range $0 \le r, s, \xi \le 1$. Then this blending curve is applied to the Eq. (5).

The velocity induced by a vortex filament with circulation Γ is given by the usual cutoff approach, which was formulated by Moore[12] and Rosenhead.[13] It is defined as

$$V = \frac{1}{4\pi} \int_c \frac{r}{(|r|^2 + \mu^2)^{\frac{3}{2}}} \times \Gamma \frac{\partial y(\xi, t)}{\partial \xi} \, d\xi \tag{8}$$

Here $y(\xi, t)$ is the position vector of a material point denoted by the Lagrangian variable ξ at an instant, which describes a vortex filament with circulation Γ. The Rosenhead cutoff parameter μ is used to remove the singularity problem in the Biot–Savart law in the region very close to the vortex filaments.

In this approach, there is no nonphysical assumption about the inner wake rollup. It is theorized that the computation of the lattice convection is able to correctly predict the inner wake rollup and the tip-vortex concentration. No distinction is made between the inner and outer filaments, which are thus considered to be potential interacting vortices. The trajectory of the tip vortex is recalculated based on the results of the time-marching free-wake analysis. The tip vortex is represented as the centroid of all the vortex filaments outboard of the maximum circulation filament.

Slow Rotation Method

The impulsive rotation method of free-wake calculation causes nonphysical strong instability of the initial wake. In such a case, the wake becomes unstable after a few spirals of the wake, as shown in Fig. 3. The direction of the vortex in the inner sheet is clockwise, which is opposite to that of the tip vortex. Therefore the vortices located near the root of the inner sheet tend to move upward due to the induced velocity from the other vortices in the inner sheet located near the tip. The inner sheet vortices near the root are also influenced by the downward velocity induced by the tip vortex and the other inner sheet vortices located near the root. The influence of the upward velocity is stronger than that of the downward velocity, and the root vortices move upward at the beginning of the early stage. After several revolutions, most of the early developed vortices move downward and the effect of downward induced velocity on the rotor increases due to the vortices located downstream. Thus, the root vortex moves downward also, as shown in Fig. 3d, but still, the location of the tip vortex is disturbed due to the root vortex moving downward. The strong shed vortices and the inner sheet vortices are generated at the initial stage as shown in Fig. 3d.

One of the key points to overcome these nonphysical phenomena is that the rotation speed is increased slowly from zero to the required speed. The rotational speed can be assumed to increase slowly from zero following the hyperbolic tangent function. The hyperbolic function is employed to model a slowly starting rotor. Then the strength of the initial wake is weak and it turns out that the downward velocity is stronger than the upward velocity.
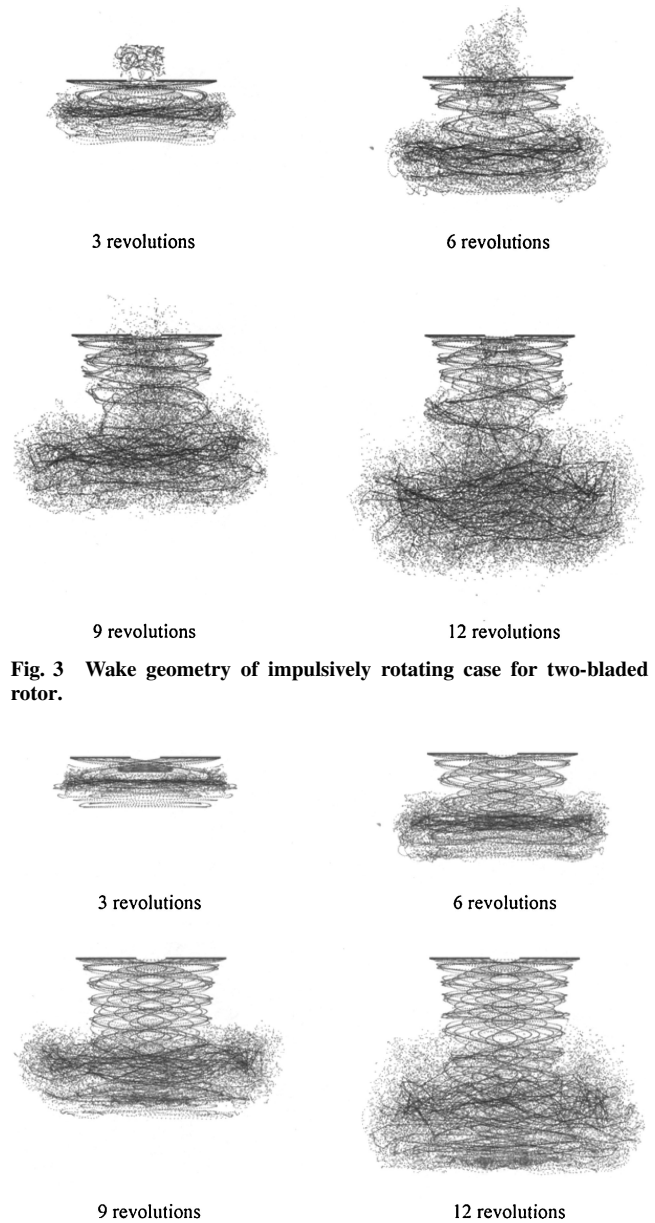

3 revolutions   6 revolutions

9 revolutions   12 revolutions

Fig. 3 Wake geometry of impulsively rotating case for two-bladed rotor.

3 revolutions   6 revolutions
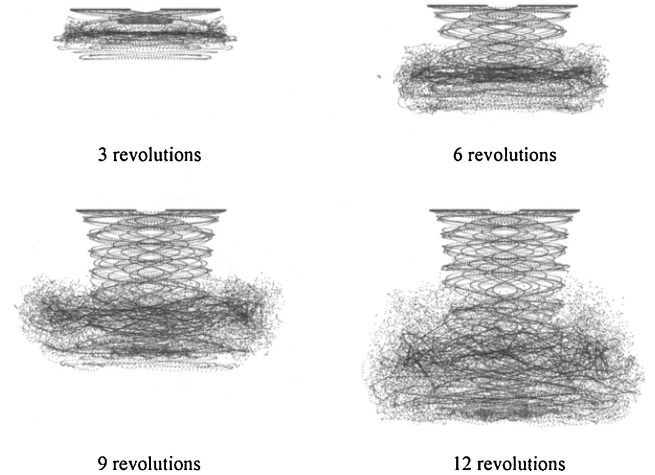
9 revolutions   12 revolutions

Fig. 4 Wake geometry of slowly starting case for two-bladed rotor.

Thus, the wake moves slowly downward from the beginning, and the disturbance of the wake is suppressed, as shown in Fig. 4, which results in the regular pattern of the wake geometry. This slowly starting approach is critical to the simulation of the rotor wake.

Acoustic Fields

The acoustic field due to the flow fluctuations can be described as follows:

$$\frac{1}{a_0^2} \frac{\partial^2 p}{\partial t^2} - \nabla^2 p = q \tag{9}$$

where p is the acoustic pressure, a_0 is the ambient acoustic velocity, and q is the acoustic source term. At low Mach number, Lighthill proposed the acoustic source term $q \approx \rho_0 \partial^2 v_i v_j / \partial x_i \partial x_j$, where v is the velocity vector of an incompressible flow and ρ_0 is the density of the ambient fluid. By using the free-space Green function $G(x, y, t - \tau)$, the solution of the equation (9) in the integral form can be obtained as
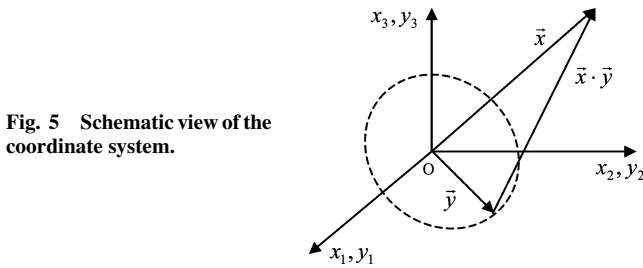
$$p(x, t) = \int G(x, y, t - \tau) q(y, \tau) \, d^3y \, d\tau \tag{10}$$

Fig. 5   Schematic view of the coordinate system.

where $\tau = t - |x - y|/a_0$ is the retarded time, x is the observation position vector, and y is the acoustic source position vector, as shown in Fig. 5.

Möhring[9] introduced the Green function vector $G(x, y, t - \tau)$ satisfying the relation $\nabla_y G = \nabla_y \times G$ and obtained the final form of Eq. (10) for low-Mach-number flows in the far field:

$$p(x, t) = \frac{\rho_0}{12\pi a_0^2 x^3} \frac{\partial^3}{\partial t^3} \int (x \cdot y) y \cdot (\omega \times x) \, d^3 y \qquad (11)$$

where $x = |x|$ and ω is the vorticity in the flowfield. Equation (11) can be expressed compactly for the vortex filament as

$$p(x, t) = \frac{\rho_0}{12\pi a_0^2} \sum_{i,k} \frac{\dddot{Q}_{ik} (t - x/a_0) x_i x_k}{x^3} \qquad (12)$$

with

$$Q_{ik} = \int y_i (y \times \omega)_k \, d^3 y = \Gamma \int y_i (y \times dy)_k \qquad (13)$$

where Γ denotes the circulation of the vortex filaments, and dy is a curve element in the tangential direction of the vortex filament. $\dddot{Q}_{ik}$ denotes the third-order derivative of Q_{ik}. The only nonvanishing components of Q_{ik} are its diagonal elements Q_{11}, Q_{22}, and Q_{33}, which additionally satisfy the relation $Q_{11} + Q_{22} + Q_{33} = 0$ of vanishing trace. The three components of Q_{ii} are related to the acoustic pressure in the three axis directions.

Validations

Tip-Vortex Pairing Prediction by Using a Time-Marching Free-Wake Method

The rotor used in this wake calculation is a subscale AH-1G model with a 41-in. radius rotating at 1800 rpm. The blade is modeled using 5 chordwise panels and 10 spanwise panels. The distribution of the spanwise panels is modeled by a quarter sine function that is clustered at the tip of the rotor. This rotor is the same as that used in the experiments of Caradonna et al. and Komerath et al.[6] Twenty-four time steps are taken per blade revolution and the vortex core radius is 10% of the chord length that is commonly used in rotor wake simulations.[14]

The tip-vortex pairing process is quantified using the trajectory tracking method. The trajectories of the tip vortices for the collective angle of 11 deg at a climb rate of 3.5 ft/s are shown in Fig. 6. The tip-vortex trajectories from the two blades are offset by 180 deg and it is clear that they are influencing each other. The first crossing of the z/R (axial direction) curves of the two vortices indicates the beginning of the vortex pairing process. The subsequent crossings indicate the rotation of the two vortices about each other. In this case, the results of the time-marching free-wake method show good agreement with the experimental data, and it is validated that the tip-vortex pairing occurs at $\varsigma = 720$ deg, just as observed in Ref. 6.

These trajectories clearly show that the local radial expansion is the result of adjacent tip vortices beginning to pair together and rotate about each other.

Sound Radiation from Mutual Threading of Two Circular Vortex Rings

In this section, the preceding numerical schemes are used to compare the numerical and the existing analytic solutions of the radiated
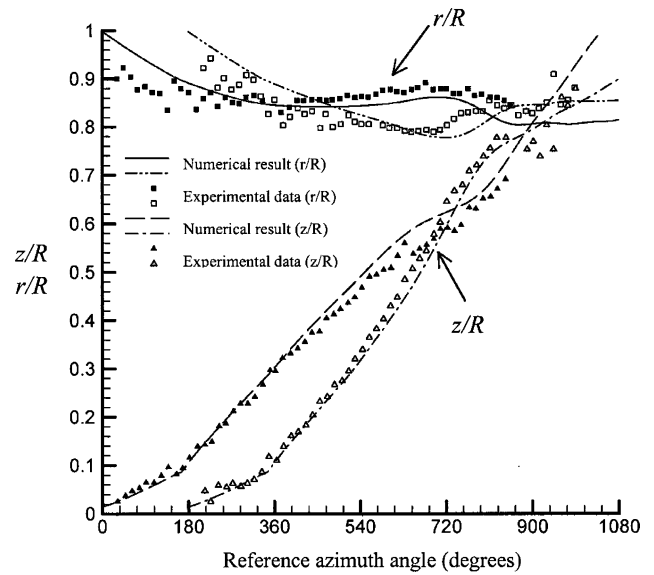
Fig. 6   Wake geometries at 11-deg collective angle, 3.5-fps climb rate (experimental data from Ref. 6).
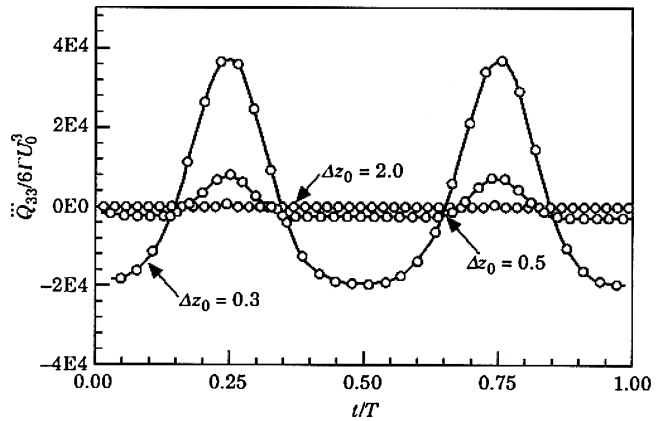
Fig. 7   Comparison of the acoustic signals by mutual threading motion: ——, analytic and ○, present.

sound owing to the interaction between two circular vortex rings. Figure 7 shows exact agreements between the numerical and the analytic solutions.

Kambe and Minota[8] calculated the acoustic field due to the mutual threading and head-on collision of the two circular vortex rings analytically using Dyson's formula.[15] To verify the present numerical method, the mutual threading problem is calculated. Two identical vortex rings are initially chosen to have the same values of the strength $\Gamma = \Gamma_1 = \Gamma_2$, the radius $R_0 = R_1 = R_2$, the core radius $c_0 = c_1 = c_2$, and the initial separation $z_1 - z_2 = \Delta z_0$. The numerical results of the acoustic pressure at farfields for the mutual threading case are compared with the analytical results in Fig. 7. The acoustic pressures $\dddot{Q}_{33}$ in Eq. (12) are scaled by $6\Gamma U_0^3$ for different initial distances of $\Delta z_0/R_0 = 0.3$, 0.5, and 2.0 respectively. Here, $U_0 = \Gamma/4\pi R_0$. The periods of the corresponding $\Delta z_0/R_0$ and $T/(R_0/U_0)$ are 0.130, 0.328, and 3.860, respectively, as analyzed in Ref. 8.

The acoustic field is closely related to the vortex position at each time step, as indicated in Eqs. (12) and (13). The velocity at a vortex filament with circulation Γ is given by Eq. (8). The Rosenhead cutoff parameter $\mu(t) = 2\delta_R c(t)$ is proportional to the core radius $c(t)$. The coefficient δ_R depends on the vorticity distribution across the core of the vortex filament. The authors choose $\delta_R = (1/2) \exp(-A - 1/2)$ with $A = 1$. As indicated in Eq. (8), the dynamics of the filament is very dependent on the core size $c(t)$ and the initial configuration of the filament $y(\xi, t = 0)$. The initial core radius c_0 is 0.05 for

the analytic solution.[8] The corresponding core radius used in the Moore–Rosenhead formula is 0.10542.

The vortex strength, time step, and number of vortex elements are the same as those of the rotor wake calculations.

Results

Mechanism of Tip-Vortex Pairing

The computed trajectories of the tip vortices are shown in Fig. 8. Figure 8a shows the three-dimensional view of the tip-vortex trajectories, and Fig. 8b shows the cross-section view of it.

Figure 9 shows the tip-vortex pairing process obtained at a collective angle of 11 deg and at a climb of 9.6 fps. In this figure, vortex 3 begins to pair with 4. This process continues until 3 and 4 interchange their positions while moving downstream. The tip-vortex pairing consists of a turn of the tip vortex from one blade rolling
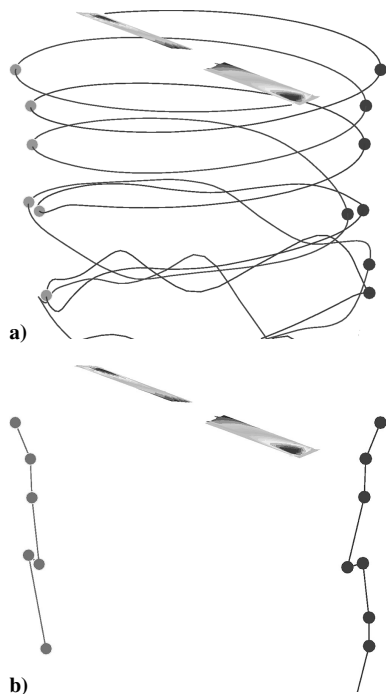

Fig. 8 Three-dimensional view and cross-sectional view of predicted wake geometries at 11-deg collective angle and 9.6-fps (2.926 m/s) climb rate: a) three-dimensional overall view and b) cross-sectional view.
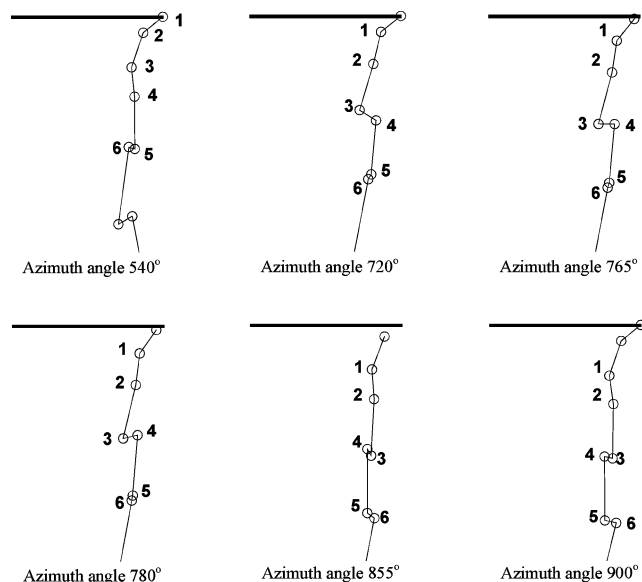

Fig. 9 Predictions of tip-vortex pairing process at 11-deg collective angle and 9.6-fps (2.926 m/s) climb rate.
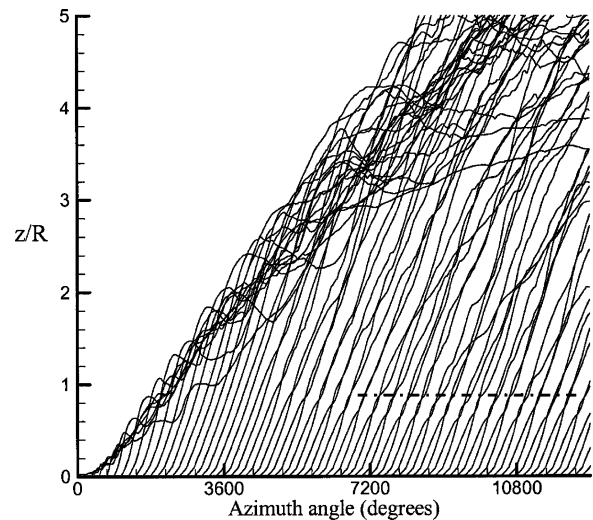

Fig. 10 Detailed tip-vortex geometry during 35 revolutions at 11-deg collective angle and 3.5-fps (1.067 m/s) climb rate.

around the tip vortex from the other blade, as shown in Fig. 1, even though different operation conditions are employed in this case.

Figure 10 shows the time history of the tip-vortex locations in a fixed cross-section plane (see Fig. 5b) during 35 revolutions from the startup. The dashed line in Fig. 10 indicates the upper boundary of converged geometries of the tip vortices. It appears that, at the beginning of the solution process, the initial vortices merge together into a bundle of starting vortices (see Figs. 4a–4d). Then these starting vortices roll about one another and convect away from the rotor at a speed (the inverse of the curve slope in the Fig. 10) lower than the individual vortex convection speed, and their motions become increasingly chaotic as time passes. Thus the initial wakes in the downstream ultimately become unstable, unsteady, or chaotic at a certain distance from the rotor.[16,17]

Tip–Vortex Noise

The noises generated by the tip vortices are calculated by using Eq. (11) presented by Möhring.[9] Möhring described the quadrupole source with third time derivative of a quantity including the circulation of the vortex and the position of the vortex as shown in Eq. (11). Therefore for constant circulation, the variation of the vortex position is very sensitive to the farfield acoustic pressure. How aerodynamic sound is generated as a result of movement of vortices, or of vorticity, in an unsteady fluid flow is explained by Powell.[7] Changes in circulation of a bound vortex ring give rise to dipole sound and the movements of vorticity in a free flow induce quadrupole sound radiation. In the pairing process, the circulation of the tip vortex is almost constant and the dominant factor in sound generation is the unsteady tip-vortex movements. Therefore, once there is vortex pairing, which causes vortex movement in the radial and axial directions due to the induced velocity of the vortex relative to the other vortex, quadrupole noise can be generated very efficiently. The strength and geometries of the tip vortex are obtained from the results of the time-marching free-wake analysis. Assuming that the tip vortices are dissipated out after the vortex pairing, the tip vortices located in the range $z/R < 1.0$ are used in the noise calculation.

Figure 11 shows the noise signals at various positions in time domain. The noises of the nonpairing case are from the tip-vortex rotation only and those of the pairing case are from the tip-vortex pairing as well as the tip-vortex rotation. From the Fig. 11, one can notice that the tip-vortex pairing amplifies the noise amplitude and generates new dominant frequencies, as shown in Figs. 11c and 11d.

The noise spectrums of Fig. 11c are shown in Fig. 12. Under the nonpairing condition, the dominant frequency is 60 Hz, as shown in Fig. 12a. In Fig. 12b, under the pairing condition, 30- and 90-Hz components increase significantly in comparison with Fig. 12a. From Fig. 9, one can know that the period of tip-vortex pairing
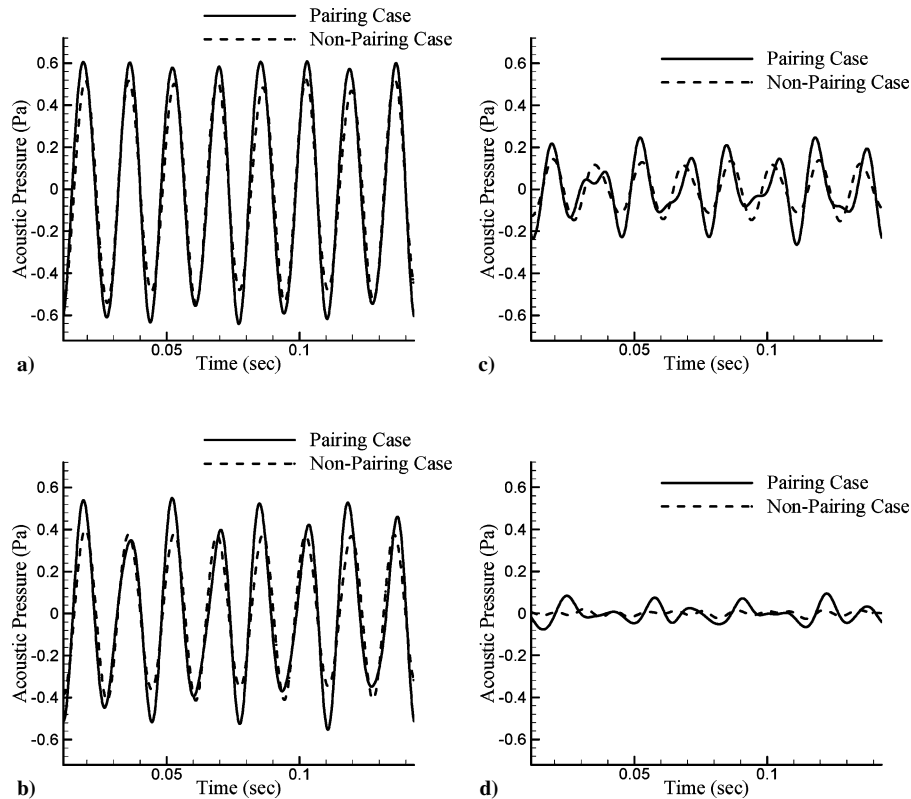
Fig. 11 Noise generated by tip-vortex in time-domain at $r = 50R$: a) $\varphi = 0$ deg, b) $\varphi = 30$ deg, c) $\varphi = 60$ deg, and d) $\varphi = 90$ deg.
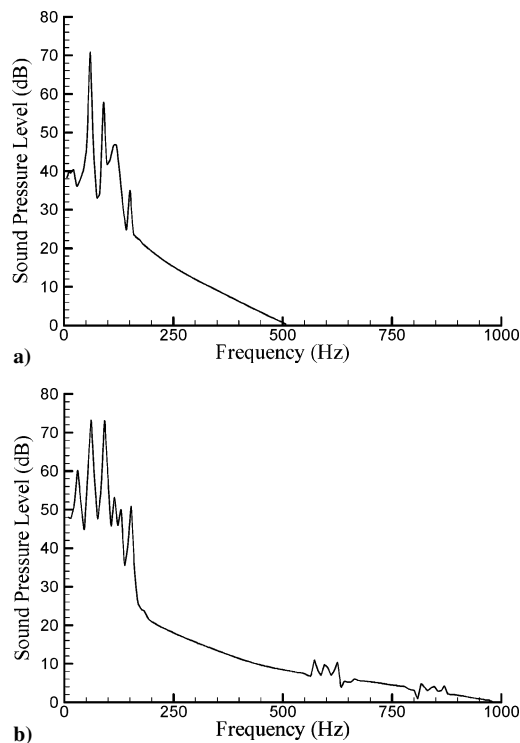

Fig. 12 Noise signal at $r = 50R$ and $\varphi = 30$ deg in frequency domain: a) nonpairing condition and b) pairing condition.

Fig. 13 Directivity patterns of 30 and 90 Hz in pairing case.

is one revolution (30 Hz). So the tip-vortex pairing increases the 30-Hz frequency component in the noise. The 90-Hz frequency component comes from the perturbation in the tip-vortex pairing process. Gupta and Loewy[4] showed analytically that the two helical vortex filaments can diverge when they meet waves with wave numbers of 1, 3, 5, and so on. The wave number is defined as the numbers of waves per revolution. Before Gupta and Loewy's work,[4] Widnall[3] showed that the pairing modes occur due to perturbations
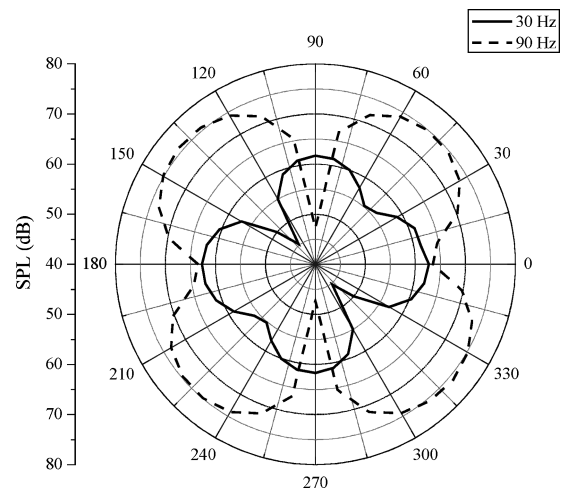
that have wave numbers of 3/2 and 5/2 for a single helical vortex filament. It can be inferred that, for the case of two helical vortices, pairing modes occur due to wave numbers 3 and 5. The frequencies of these wave numbers are 90 and 150 Hz in the present case. Figure 13 shows the directivities of the 30- and 90-Hz components in the wake noises. When pairing occurs, directivities of the 30- and 90-Hz components show the quadrupole characteristics. The 30-Hz noise component increased by the pairing period radiates to the direction of the rotation axis (90, 270 deg) and the rotation plane (0, 180 deg). The 90 Hz noise component increased by the instability perturbations radiates to 45-, 135-, 225-, and 375-deg directions.

Tip-Vortex Noise vs Rotor Noise

The pairing phenomenon causes unsteady fluctuations in the blade force and these fluctuations increase the noise of the blade. But because the flight condition that is used in the noise calculation
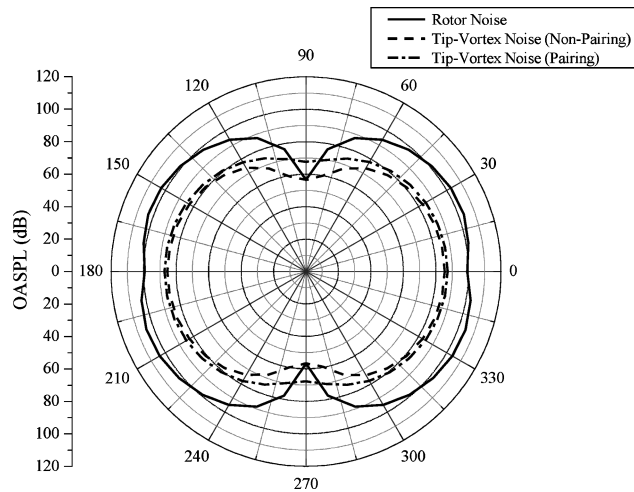
Fig. 14   Comparisons of OASPLs.

is the climbing flight case, the unsteady fluctuations due to the pairing do not exist. Figure 14 shows the overall sound pressure level (OASPL) of the rotor noise and the tip-vortex noises. The rotor noise is calculated using the Lowson equation with the calculation of unsteady rotor force. It is revealed that the tip-vortex noise is louder than the rotor noise by 10 dB in the direction of the rotation axis (90 and 180 deg) when the pairing occurs, whereas the rotor noise governs the other directions. The reason that the tip vortex noise is louder than the rotor noise is that the rotor loading is almost steady. Therefore, there is no efficient sound radiation in the direction of the rotor axis, that is, 90 deg in Fig. 14. On the other hand, vortex noise exists in the direction shown in Fig. 13.

Conclusions

In this paper, the generation and radiation of the rotor tip-vortex pairing noise were investigated numerically. The wake geometries of a two-bladed rotor in axial flight are calculated using the time-marching free-wake method without a nonphysical model of the far wake. The acoustic field is obtained by using the acoustic analogy. The accuracy of the present calculation is validated by comparing the present results with the experimental data and the analytic solutions. The main results can be summarized as follows:

1) Tip-vortex pairing noise is greater than rotor noise in the direction of the rotation axis.

2) Tip-vortex pairing noise has a quadrupole directivity pattern.

3) Peak components of the noise spectrum represent pairing period and instability mode.

References

[1]Landgrebe, A. J., "The Wake Geometry of a Hovering Helicopter Rotor and Its Influence on Rotor Performance," *Journal of the American Helicopter Society*, Vol. 17, No. 4, 1972, pp. 3–15.

[2]Tangler, J. L., Wohlfed, R. M., and Miley, S. J., "An Experimental Investigation of Vortex Stability, Tip Shapes, Compressibility, and Noise for Hovering Model Rotor," NASA CR-2305, Sept. 1973.

[3]Widnall, S. E., "The Stability of a Helical Vortex Filament," *Journal of Fluid Mechanics*, Vol. 54, No. 4, 1972, pp. 641–663.

[4]Gupta, B. P., and Loewy, R. G., "Theoretical Analysis of the Aerodynamic Stability of Multiple, Interdigitated Helical Vortices," *AIAA Journal*, Vol. 12, No. 10, 1974, pp. 1381–1387.

[5]Martin, P. B., Bhagwat, M. J., and Leishman, J. G., "Strobed Laser-Sheet Visualization of a Helicopter Rotor Wake," *Journal of Flow Visualization and Image Processing*, Vol. 7, No. 1, 2000, pp. 31–50.

[6]Caradonna, F., Hendley, E., Silva, M., Huang, S., Komerath, N., Reddy, U., Mahalingam, R., Funk, R., Ames, R., Darden, L., Villareal, L., Gregory, J., and Wong, O., "An Experimental Study of a Rotor In Axial Flight," AHS Specialists' Meeting on Aerodynamics and Aeroacoustics, AHS International, Alexandria, VA, Oct. 1997.

[7]Powell, A., "Theory of Vortex Sound," *Journal of the Acoustical Society of America*, Vol. 36, No. 1, 1964, pp. 177–195.

[8]Kambe, T., and Minota, T., "Sound Radiation from Vortex System," *Journal of Sound and Vibration*, Vol. 74, No. 1, 1981, pp. 61–72.

[9]Möhring, W., "Sound Radiation by Two Elliptic Vortex Rings," *Journal of Sound and Vibration*, Vol. 140, No. 1, 1990, pp. 155–162.

[10]Ryu, K. W., and Lee, D. J., "Sound Radiation from Elliptic Vortex Rings: Evolution and Interaction," *Journal of Sound and Vibration*, Vol. 200, No. 3, 1997, pp. 281–301.

[11]Na, S. U., and Lee, D. J., "Numerical Simulations of Wake Structure Generated by Rotating Blades Using a Time-Marching Free-Vortex-Blob Method," *European Journal of Mechanics*, Vol. 18, No. 1, 1999, pp. 147–159.

[12]Moore, D. W., "Finite Amplitude Waves on Aircraft Trailing Vortices," *Aeronautical Quarterly*, Vol. 23, Feb. 1972, pp. 307–314.

[13]Rosenhead, L., "The Spread of Vorticity in the Wake Behind a Cylinder," *Proceedings of the Royal Society, Series A*, Vol. 127, 1930, pp. 590–612.

[14]Leishman, J. G., Baker, A., and Coyne, A., "Measurements of Rotor Tip Vortices Using Three-Component Laser Doppler Velocimetry," *Journal of the American Helicopter Society*, Vol. 41, No. 4, 1996, pp. 342–353.

[15]Dyson, F. W., "The Potential of an Anchor Ring, Part II," *Philosophical Transactions of the Royal Society of London, Series A*, Vol. 184, 1893, pp. 1041–1106.

[16]Chung, K. H., Na, S. U., Jeon, W. H., and Lee, D. J., "A Study on Rotor Tip-Vortex Pairing Phenomena by Using Time-Marching Free-Wake Method," *Proceedings of American Helicopter Society 56th Annual Forum*, AHS International, Alexandria, VA, 2000.

[17]Chung, K. H., and Lee, D. J., "Numerical Prediction of Rotor Tip Vortex Roll-up in Climb Flight by Using a Time-Marching Free-Wake Method," *Computational Fluid Dynamics Journal*, Vol. 12, No. 1, 2003, pp. 80–88.

H. Atassi
Associate Editor